J. Fluid Mech. (1980), *vol.* 96, *part* 1, *pp.* 133–157
Printed in Great Britain

Droplet motion induced by weak shock waves

By SAMUEL TEMKIN AND SUNG SOO KIM†

Department of Mechanical, Industrial, and Aerospace Engineering,
Rutgers University, New Brunswick, New Jersey 08903

(Received 27 June 1977 and in revised form 22 January 1979)

An experimental study of the motion of small water droplets in a shock tube is reported. Droplet displacement data were obtained by means of reflected-light stroboscopic illumination for droplet diameters in the range 87–575 μm, and for shock strengths, $\Delta P/P_1$, in the range 0·0018–0·3. The displacement data are fitted by means of best-fit polynomials in time, which are used to compute droplet velocities, accelerations, and drag coefficients. All of our drag coefficient data have values which are larger than the steady drag at the same Reynolds numbers. The differences are attributed to time changes of the relative fluid velocity U_r. This may affect the size of the recirculating region and, therefore, the drag. In particular, it is argued that the drag is larger or smaller than the steady drag, depending on whether the dU_r/dt is negative or positive, respectively. Our experiments, which were performed for $dU_r/dt < 0$, confirm this expectation. Furthermore, it is shown that the difference between steady and transient drag coefficients, at the same Reynolds number, depends only on the value of a parameter $A = (\rho_p/\rho_0 - 1)(D/U_r^2)(dU_r/dt)$. Here ρ_p and ρ_0 are the densities of the droplets and of the surrounding gas, respectively, and D is the droplet diameter. In fact, in the Reynolds number range $3{\cdot}2 < Re < 77$, where multiple data are available having the same value of Re but having different values of A, the drag data can be expressed as $C_D = C_{DS}(Re) - KA$, where $C_{DS}(Re)$ is the steady drag at the instantaneous Reynolds number Re, and K is a constant of order 1.

1. Introduction

Situations in which small particles move in fluids often occur in a wide variety of natural and man-made flows. In some of these, the motion of the particles plays an important role. For example, in rainclouds, the relative motion between cloud droplets that is induced by external fields, or by internal fluid forces of viscous origin, affects the efficiency of collisions between droplet pairs and, therefore, affects the droplet growth rate (Langmuir 1948; Saffman & Turner 1956; Mason 1971). Similarly, the relative motion between particles and carrier gas in rocket nozzles affects the rocket performance (Hoglund 1962; Marble 1963).

In order to understand some of the mechanical aspects of a fluid–particle system, one usually has to determine the particle's motion relative to the carrier fluid. This requires a knowledge of the forces with which the fluid acts on the particles. Usually, these forces are expressed in terms of a drag coefficient, C_D. In the case of steady motion of rigid particles, this coefficient depends only on the Reynolds number, Re. The functional dependence of C_D on Re has been determined analytically only for spherical

† Present address: Ingersoll Rand Research, Princeton, N.J.

0022-1120/80/4344-7920 $02.00

particles moving steadily at very small Reynolds numbers. For other values of that parameter, C_D has been determined experimentally using a variety of techniques that lend themselves to steady measurements, such as measurements of terminal velocities of spheres falling in liquids. The results of many such measurements cover a wide range of Reynolds numbers and are collectively known as the 'standard drag coefficient'. Although these measurements are quite reliable, they are applicable only to rigid spheres moving steadily in a fluid. In most real situations, however, the relative motion between sphere and fluid is unsteady, owing to unsteady external forces, or to accelerations of the fluid in which the spheres are embedded. Under such conditions, the forces on a sphere do not depend on the Reynolds number alone. Similarity arguments show that, then, the drag coefficient depends also on the relative acceleration between fluid and sphere. However, at present this dependence is poorly understood. For example, some authors have reported that the drag coefficient increases with acceleration (e.g. Lunnon 1926; Karanfilian & Kotas 1978); whereas others report the opposite effect (Ingebo 1965; Roos & Willmarth 1971). Further, some authors report that acceleration is of no importance (Rudinger 1963; Selberg & Nicholls 1968) and ascribe the measured departures of C_D from the standard value to effects other than acceleration.

In addition to the experimental studies mentioned above, there are several others that have also treated the effects of acceleration. The literature on the subject was reviewed by Torobin & Gauvin in 1960, who concentrated on studies related to solid particles. Earlier, Hughes & Gilliland (1952) had reviewed the literature on the mechanics of droplets. More recent experimental studies of spheres accelerating in fluids include some of those already mentioned, and those of Odar & Hamilton (1964), Hill (1973) and Reichman (1973).

On the theoretical side, there have also been several studies dealing with accelerated motion, but most of these consider only small Reynolds number motions. These works are based on the unsteady Stokes equations (Ockendon 1968; Temkin 1972), or on Basset's equation (Pearcey & Hill 1955) and yield results which are of limited validity. On the other hand there have recently appeared in the literature several numerical computations of the flow field around accelerating spheres which cover a much wider Reynolds number range. Included here are the works of Rimon & Cheng (1969) and of Dennis & Walker (1972). However, these works study situations in which the sphere's motion is prescribed, namely impulsive motion, whereas in most situations of practical interest the sphere motion is unknown.

In this work we report the results of an experimental investigation that was initially undertaken with the purpose of determining how single spheres respond to the highly transient flow fields that are created by the passage of a shock wave. The motivation for this work was an earlier experiment (Temkin 1970) which indicated that shock waves might induce rapid coalescence in an aerosol cloud. The effect, which was ascribed to relative motion between droplets, could not be quantified because of uncertainties associated with sphere motion in those conditions.

In the investigation reported here we have not used rigid spheres, mainly because of the difficulties associated with releasing them individually in a well-controlled fashion. Instead, we have used streams of water droplets that are produced by the well-known instability of a thin jet. However, using droplets instead of rigid spheres should bring about further departures from the standard drag because, in addition to

the internal circulation which may exist in the droplet, the droplet may deform significantly. The parameter which controls the deformation is the Weber number, *We*. This measures the magnitude of the fluid forces which tend to deform the droplets, relative to surface tension forces which tend to maintain the droplets' spherical shape. Measurements are available (e.g. Hanson, Domich & Adams 1963; Reichman & Temkin 1974) which show that, for Weber numbers of the order 3–4, water droplets in air are shattered by suddenly imposed flow fields. Below those values the droplets do not break up but oscillate with amplitudes which may be large. In this work we have performed some experiments to determine the amount of deformation below critical Weber numbers for breakup. It has been found that for a Weber number of 0·55 the maximum amplitude of the oscillation is about 0·12 initial diameters, and substantially smaller at smaller Weber numbers. Thus, a criterion for the sphericity of water droplets moving in air is that the Weber number should be smaller than these values. Somewhat arbitrarily we have chosen the value $We = 0{\cdot}15$ as giving the limit for spherical behaviour.

Other authors have used criteria based on other parameters, for example, the Reynolds number. Thus, based on steady drag measurements reported by Beard & Pruppacher (1969), Pruppacher, Le Clair & Hamielec (1970) assumed that, for Reynolds numbers smaller than 200, water droplets could well be approximated as rigid spheres. This criterion is, for the data of Beard & Pruppacher, consistent with ours because the Weber number corresponding to those data were small.

The main part of this investigation consists of measurements, in a shock tube, of water droplet displacements responding to the passage of weak shock waves. Another part relates to droplet deformation under the effects of the waves and will be reported separately. The droplets' diameters used in our work ranged from 87 to 575 μm, and the shock strengths varied from 0·0018 to 0·3. The corresponding Reynolds and Weber numbers varied from 1·2 to 952, and from 0·001 to 4, respectively. The displacement data are fitted by means of third degree polynomials in time. These are used to obtain droplet velocities and accelerations. Drag coefficients were obtained from these derived quantities by means of the usual definition of C_D. However, in order to reduce the effects of deformation, we used only data with Weber numbers less than 0·15, although, in effect, most of our data have even smaller Weber numbers.

Our drag coefficients have, in all cases, larger values than the standard drag. In the larger Reynolds number range the differences are small, but increase with decreasing Reynolds numbers. The departures from the standard drag-curve are similar in nature to those found by other investigators, but are of smaller magnitudes and correspond to lower Reynolds numbers.

Arguments are given in terms of the fluid velocity, relative to an observer moving with the sphere, which indicates that when this relative velocity increases in time, the drag should be smaller than the steady, and that, when it decreases in time, the drag should be higher than the steady. In our tests we always have $dU_r/dt < 0$, where U_r is the magnitude of the relative velocity, so that for the same Reynolds number our drag should be larger than the steady drag. To test this prediction one should observe the variations of C_D *versus* acceleration for fixed Reynolds numbers. Unfortunately, our results contain only relatively few data points having equal Reynolds numbers but different values of the relative acceleration. Nevertheless, these data display the trend that is predicted by our relative-velocity arguments. Also, they show that

the difference between transient and steady values depends only on the relative acceleration. We therefore conclude that the differences between our drag results and those given by the standard drag are due to unsteady effects associated with the recirculating region in the rear of the sphere. However, this conclusion should be tested by additional experiments in which the relative acceleration dU_r/dt can have both positive and negative values.

2. Droplets' equation of motion

Here we obtain a relation for the drag coefficient, C_D, and for the Reynolds number, Re, in terms of the data that are measured in our experiments. The basic equation is, of course,

$$m_p \frac{d\overline{U}_p}{dt} = \overline{F}_e + \overline{F}_f. \tag{1}$$

Here $m_p = (\pi/6) D^3 \rho_p$ is the mass of the droplet, ρ_p its density, D its diameter, and $\overline{U}_p$ its velocity. The quantities on the right-hand side represent, respectively, the external forces and the fluid forces acting on the sphere. In our experiments the only external force is that due to gravity. Thus $\overline{F}_e = m_p \bar{g}$, where $\bar{g}$ is the acceleration due to gravity. The forces on the sphere due to the surrounding fluid are usually expressed in terms of a drag coefficient C_D. Since in our experiments both the droplets and the surrounding fluid are in motion, it is convenient to use, in the definition of C_D, the relative velocity between fluid and sphere. Thus, if the velocity of the fluid is denoted by $\overline{U}$, we have

$$\overline{F}_f = C_D \frac{\pi D^2}{4} \tfrac{1}{2} \rho_0 |\overline{U} - \overline{U}_p| (\overline{U} - \overline{U}_p). \tag{2}$$

Two points arise in regard to this definition. First, the definition assumes that all of the fluid forces can be taken into account by means of C_D. That this is not the case may be easily seen by considering the case of very small Reynolds number unsteady flow. Here, as is well known, the fluid forces are due to a viscous drag, to an acceleration reaction and to 'history' effects. Thus, the best that can be said about C_D as defined above is that it represents, instantaneously, the combined effects of several types of fluid forces, some of which depend on the entire history of the motion. The second point about (2) is that it contains a fluid velocity $\overline{U}$ whose meaning should be clarified. For one-dimensional flows, this velocity would represent the fluid velocity far from the sphere. For other cases, this definition is useless. Perhaps a better definition for $\overline{U}$ is that it represents the velocity that the fluid would have at the instantaneous location of the sphere's centre, had the sphere not been there. With these points in mind, we may write for (1)

$$m_p \frac{d\overline{U}_p}{dt} = m_p \bar{g} + C_D \frac{\pi D^2}{4} \tfrac{1}{2} \rho_0 |\overline{U} - \overline{U}_p| (\overline{U} - \overline{U}_p). \tag{3}$$

In our experiments, the droplets move in a plane. Thus, if we let the x and y axes of a Cartesian system of co-ordinates fall on that plane, then the x and y components of (3) are, respectively,

$$m_p \frac{du_p}{dt} = C_D \frac{\pi D^2}{4} \tfrac{1}{2} \rho_0 |\overline{U} - \overline{U}_p| (u - u_p), \tag{4}$$

$$m_p \left(\frac{dv_p}{dt} + g \right) = C_D \frac{\pi D^2}{4} \tfrac{1}{2} \rho_0 |\overline{U} - \overline{U}_p| (v - v_p). \tag{5}$$

Here u_p and v_p are the x and y velocity components of the droplet, and u and v the respective velocity components of the fluid. One of these fluid-velocity components may be eliminated. Thus, dividing (4) by (5) and solving for v we obtain

$$v = v_p + (u - u_p)\frac{dv_p/dt + g}{du_p/dt}. \tag{6}$$

This gives, for the magnitude of the relative velocity,

$$|\bar{U} - \bar{U}_p| = (u - u_p)\frac{[(du_p/dt)^2 + ((dv_p/dt) + g)^2]^{\frac{1}{2}}}{du_p/dt}, \tag{7}$$

and, for C_D,

$$C_D = \tfrac{4}{3}D\frac{\rho_p}{\rho_0}\frac{(du_p/dt)^2}{(u - u_p)^2[(du_p/dt)^2 + ((dv_p/dt) + g)^2]^{\frac{1}{2}}}. \tag{8}$$

This equation expresses C_D in terms of quantities which may be determined experimentally.

The results for C_D are usually given in terms of the Reynolds number Re. This, in turn, is defined as usual, but with the relative velocity magnitude $|\bar{U} - \bar{U}_p| = U_r$, playing the role of the characteristic velocity. Thus,

$$Re = \frac{\rho_0 |\bar{U} - \bar{U}_p| D}{\mu}, \tag{9}$$

where $|\bar{U} - \bar{U}_p|$ is given by (7).

3. Experimental apparatus and measurements

The main components of the experimental apparatus used in this work were a horizontal shock tube, a droplet generator and a high speed photographic system. Some of the instrumentation used with these components is shown schematically in figure 1. The apparatus is briefly described below. A more detailed description may be found elsewhere (Kim 1977).

3.1. *Shock tube*

A conventional shock tube facility was selected for our experiments because it provides easily controlled transient flows that have fairly uniform fluid velocities over a relatively large volume. The tube was made of aluminium and had a circular cross-section with an inside diameter of 6·35 cm, and with a length of 511 cm. The length of the driver section, 183 cm, and the distance between test section and the end of the tube were selected to maximize the test time for a tube of that length. For the conditions existing in our tests, the maximum test time was 10·8 ms, nearly equal to the ideal test time that is predicted by linear theory, $2L_d/a_1$, where L_d is the driver's length and a_1 is the speed of sound in the driven section.

In our droplet displacement experiments it was required that the shocks be weak. One of the reasons for this requirement was that we wanted to minimize droplet deformation. In principle, this could be achieved by simply reducing droplet size. However, it was found that, below a certain size, it became very difficult to produce droplets in a controlled manner. Now, in order to produce weak shocks in a shock tube, one requires small pressure differences between driver and driven sections. This necessitated the use of thin diaphragm material. In our earlier tests we used diaphragms

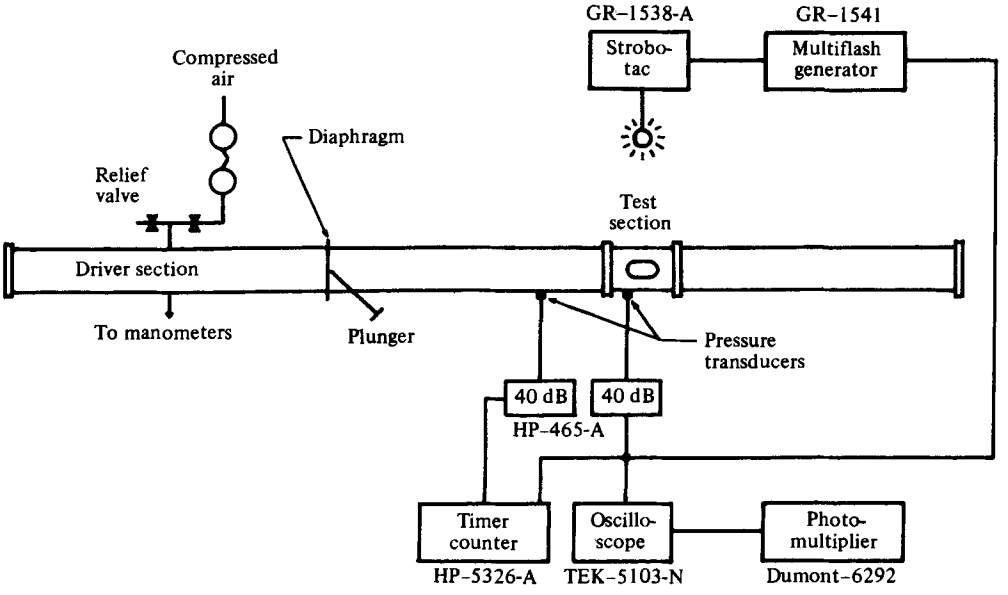

FIGURE 1. Experimental apparatus.

made of commercially available cellophane film having a mean thickness of 0·0025 cm. This was the smallest thickness available, and was suitable for relative pressure differences, $(p_4-p_1)/p_1$, of about 0·1 or larger. For smaller values of this ratio, the diaphragms would not break up evenly. Instead, the plunger would merely make a small opening in the diaphragm, thus allowing for a slow expansion of the pressurized air. This slow expansion would not produce the desired results. To overcome this problem, the diaphragm material was annealed by placing it in an oven at a temperature of about 340 °F for about 10 min. At the end of this period, the cellophane would become very crisp. A measure of this 'crispness' was obtained by determining the energy needed to rupture the film. To this end, an Elmendorf Tearing Tester was used to rupture both treated and untreated samples. When the required energies were compared, it was found that the annealed sample required only about $\frac{1}{14}$ of the energy required by the untreated sample. Also, the annealed material would disintegrate rapidly and uniformly over the entire cross-section of the tube when acted on by the plunger. By means of this technique we were able to produce controlled weak shock waves with initial pressure-difference ratios, $(p_4-p_1)/p_1$, as low as 0·0018.

The most important flow quantity that is required in (7) is the horizontal flow velocity behind the shock wave, u_2 in the usual shock tube terminology. In conventional shock tube measurements, this quantity is obtained in terms of the shock speed by means of the normal shock equations. This procedure is adequate for sufficiently large shock overpressures, but may result in large errors otherwise. Since in our case we had very low pressure differences, we obtained u_2 by measuring actual shock overpressures with calibrated pressure transducers and by using the perfect gas normal shock relation

$$u_2 = a_1\left(\frac{p_2}{p_1}-1\right)\left(\frac{2/\gamma_1}{(\gamma_1+1)(p_2/p_1-1)+2\gamma_1}\right)^{\frac{1}{2}}. \tag{10}$$

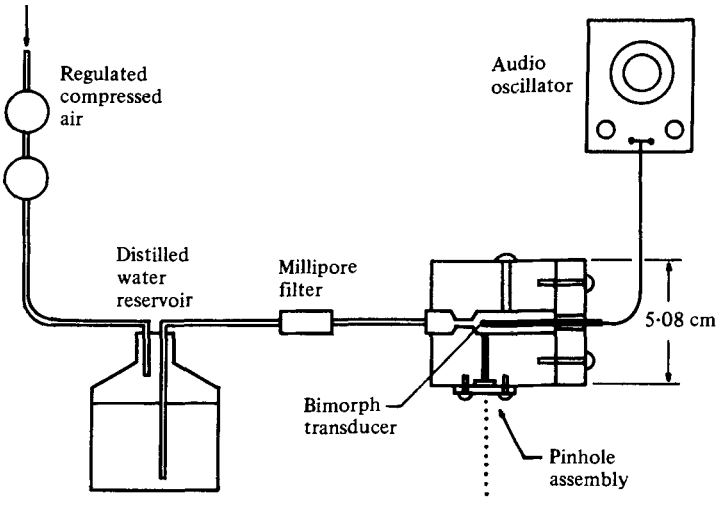

FIGURE 3. Droplet generator.

In this equation γ is the ratio of specific heats, and the subindices 1 and 2 refer, as usual, to the properties in front of and behind the shock wave, respectively.

Other flow properties that are required, such as $\rho_0 (= \rho_2)$, are also determined by means of the normal shock relations. These relations apply provided that the shock wave front is normal to the direction of propagation. Figure 2 (plate 1) shows shadowgraphs obtained in two of our tests. The circles appearing there are the shadows of water droplets falling across the tube. It may be seen that the shock fronts are fairly flat, at least in a relatively large area near the droplets where all of our measurements were made.

3.2. *Droplet generator*

The droplets required for our experiments are produced by means of the well-known capillary instability of laminar jets issuing from small orifices. In our earlier tests we used hypodermic needles to obtain the thin jets. The droplet streams that were thus produced were sometimes unstable owing to lateral vibrations of the hypodermic needle. Presently, a modification introduced by Adam, Cataneo & Semonin (1971) is being used in which the needle is replaced by a small pinhole, and where the excitation of the disturbances is provided by a LZT bimorph transducer.

Figure 3 shows a schematic diagram of the complete droplet generator arrangement. Distilled water was used to produce the droplets. Careful filtering of the water was necessary to remove suspended impurities which might obstruct the small pinhole apertures. These varied from 25 to 300 μm in diameter. Droplets thus produced had diameters ranging from 86 μm to about 600 μm. The production of the 86 μm droplets required much effort, as the 25 μm pinhole used then had to be cleaned often. Figure 4 (plate 2) shows photographs of two droplet streams thus produced. A transparent ruler with 1 mm subdivisions is included for comparison. The sizes of the droplets shown in those photographs are the smallest and the largest used in our experiments. Stable streams of intermediate sizes were also produced and used. Table 1 gives typical data related to the generation of droplet streams. The quantity d in the table

d (cm)	D (cm)	f (Hz)	λ (cm)	λf (cm s^{-1})	λ/D	ka	β
0·0025	0·0087	14500	0·029	422	3·34	0·42	2·20
0·0050	0·0133	7100	0·046	330	3·49	0·40	2·10
0·010	0·0256	4050	0·105	426	4·11	0·31	3·61
0·020	0·0469	2100	0·166	350	3·55	0·39	4·15
0·030	0·0575	1560	0·163	254	2·83	0·54	3·54

TABLE 1. Droplet generator parameters.

represents the pinhole diameter, D the droplet diameter, f the frequency of the imposed disturbance, and λ the spacing between any two consecutive droplets.

The frequencies shown in the table were chosen because they provided the most stable streams (for given pinhole diameter and jet velocity), and the largest droplet spacing. Other frequencies could also be used, but without very stable results.

Also given in that table are the initial droplets' vertical velocities, λf. These velocities are not, necessarily, terminal velocities. Rather, they more nearly correspond to the jet's exit velocities, and in most cases were larger than the terminal. For example, the terminal velocity of a 90 μm droplet in air is about 20 cm s^{-1}, whereas our 87 μm droplets were falling at velocities of the order of 400 cm s^{-1}. On the other hand, the *falling velocity of our 575 μm droplets, 254 cm s^{-1},* is nearly equal to the terminal velocity corresponding to that size.

Also given in the table are ratios of interdroplet distance to droplet diameter. It is seen that, typically, the droplet spacing is only a few droplet diameters. As will be explained later, this relatively short spacing is responsible for some inaccuracies in the drag coefficients that are computed by means of (8).

The next column in the table lists values of ka, where k is the wavenumber of the disturbance, and a is a measure of the initial jet radius (which was not measured in every test).† These numbers are consistent with Rayleigh's theory for the temporal instability of a thin jet, which indicates that axisymmetric disturbances will grow exponentially for values of ka between 0 and 1, and with maximum growth rates for $ka \approx 0{\cdot}7$. Our measured values of ka do not correspond to this maximum value because the disturbances had frequencies that were selected to increase the separation between the droplets and to increase the stability of the streams, i.e. they are a trade-off between large growth rates which, for $ka < 0{\cdot}7$, increase with frequency, and maximum separation which decreases with frequency.

Finally, the table gives values of a parameter β defined by

$$\beta = (\rho_l a/\sigma)^{\frac{1}{2}} v_j,$$

where ρ_l is the density of the liquid, and v_j is the velocity of the jet. This parameter plays an important role in the theory of capillary jet instability that was presented recently by Keller, Rubinow & Tu (1973). These authors treated the spatial instability of the jet and found that for sufficiently low values of β other more unstable modes appear. Our values of β, however, fall in the instability region where the unstable modes are basically those predicted by Rayleigh.

† The value of a is found, approximately, by equating the volume of a drop of diameter D to the volume of a cylinder of liquid of diameter $2a$ and length λ.

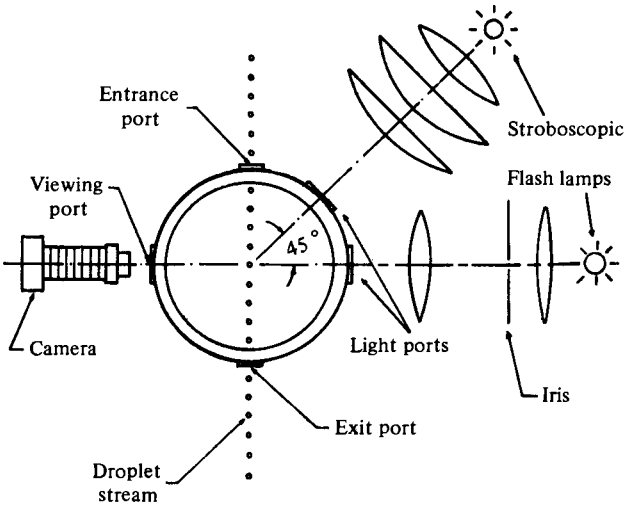

FIGURE 5. Droplet-illumination system.

3.3. *Droplet photography*

As stated earlier, the trajectories of the droplets in our experiments were planar. This enabled us to use photographic techniques to obtain displacement data. However, because of the nature of the motion, high-speed photography was required. Of the several methods available for this purpose, we selected one in which stroboscopic light, scattered by the droplets, is recorded on photographic film. The main reason for selecting this method is that it can be used to record, on a single negative, the positions of the droplets at various instants, thus enabling us to compute trajectories with relatively high accuracy. Other methods include high-speed cinephotography, and a novel technique which takes advantage of the mode of operation of focal plane shutters (Temkin & Reichman 1972). However, cinephotography yields one droplet position per frame and is, therefore, not amenable to rapid or very accurate data analysis. The other technique requires a knowledge of the droplets' vertical velocity, and in our tests this is not known *a priori*.

The technique we chose was used in conjunction with another which provides single, backlighted photographs of the type shown in figure 4. This type of photography is necessary to observe the shape of the droplets, and to determine their size. The illumination provided by this method (Koehler illumination) is very uniform in the objective field, and is largely responsible for the sharpness of the resulting photographs.

Both reflected and backlighted illumination arrangements are shown schematically in figure 5. The 135° angle for the scattered-light method was selected mainly because of ease of operation and not because of a major lobe in the scattered-intensity pattern around the droplet.

The light sources in both arrangements were the flash lamps of General Radio Stroboscopes Model 1538-A. At the setting used, these provide relatively intense flashes with a duration, at the one-third peak intensity, of less than a microsecond.

The heart of the system is an electronic unit (General Radio Model 1541 Multiflash Generator) that is capable of producing up to sixteen consecutive voltage pulses in response to an input signal. The pulses can be used to produce the same number of

flashes from the stroboscopes at specified intervals. This interval is limited only by the stroboscopes' capabilities. In our case, the time interval was set at 0·4 ms on the instrument's dial. (The exact interval was measured with a timer-counter.) Thus, the equivalent flashing rate was 2500 flashes s^{-1}.

Typical photographs obtained by the scattered-light method during a test are shown in figures 6 and 7 (plates 3 and 4). The photographs show the stream of droplets at various instants which include one before the arrival of the shock wave. The shock-induced flow is from left to right. It may be seen that all of the droplets in the droplet stream move to the right equal distances in equal times. This is indicated by the parallel positions of the stream obtained at various times. This is an important point about our measurements for it shows that the imposed fluid velocity profile, to which the droplets are responding, is uniform in the test area. Non-uniformities that might be present could be easily detected by this type of photography.

The multiflash generator was triggered by a signal from one of the pressure transducers, and its output pulses could be accurately timed in relation to the instant at which the shock wave would arrive at the location of the droplet streams. However, in order to obtain correct displacement data, it is necessary to determine whether each pulse resulted in a flash. This was done by means of a photomultiplier (Dumont Model 6292) whose output, in response to the flashes, was recorded in a storage-type cathode ray oscilloscope (Tektronix Model 5103N). The actual number of flashes could be thus counted. It was found that, in all cases, the stroboscope did not respond to the second pulse from the multiflash generator. Thus, in figures 6 and 7, there are only 15 flashes. (The brightest stream on the left of those pictures was taken prior to the arrival of the shock at a more intense setting in the stroboscope.) The fact that one of the flashes is missing is of little consequence provided that its order, among the sixteen possible flashes, is known.

Photographic negatives, such as those from which figures 6 and 7 were made, were used to determine droplet trajectories. However, while the horizontal displacement during one time interval is clearly unique, the vertical is not; that is, given a droplet location in the stream at one instant, its vertical location, the next illuminated instant, is not clearly evident in those photographs. Thus, unless special care and techniques are used, the resulting trajectories will be erroneous. We have used two techniques to determine the actual consecutive locations of the droplets. The first one makes use of the fact that, when the negatives containing the data are sufficiently enlarged, small irregularities appear in the droplet streams. For example, one or two droplets may be slightly misaligned with respect to the other droplets, and this misalignment is preserved as the droplets move. Because of this, it is possible to make a one-to-one correspondence between the droplets at two consecutive instants. The second method makes use of the fact that the initial vertical velocity of the droplets can be determined from the photographs. Thus, it is possible to estimate the distance it will travel down in one time interval, and this estimate will yield the location of the droplet at that time. This method was used only from time to time in order to test the accuracy of the other.

Figure 8 (plate 5) shows typical results of such procedures. The figure is similar to those shown earlier, except that actual droplet trajectories are superimposed on the photographic data.

Relative horizontal and vertical distances between successive points in the droplet's

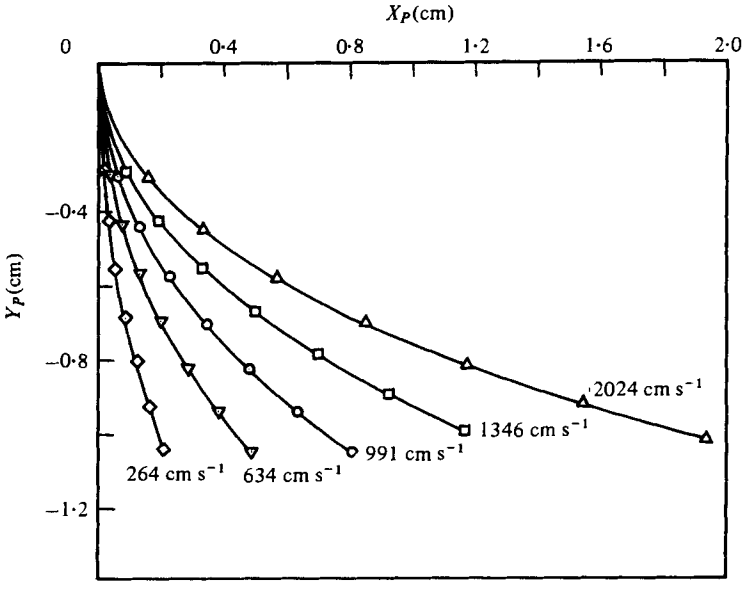

FIGURE 9. Effect of flow velocities on motion of 87 μm droplets.

trajectory were measured directly from the negatives by means of a Bausch and Lomb 25·4 cm Bench Contour Projector. This unit was equipped with a microscope that had a reticle graduated to 2 μm, and having total magnifications of either 10× or 35×. The actual distances travelled by the droplets were obtained from these measurements by taking into account the magnifications of the camera and bellows and of the measuring system. The resulting vertical and horizontal displacements, together with other pertinent data, were then digitized for later analysis.

All of the photographs were made with a Nikon F-2 camera equipped with bellows and with a 50 mm lens mounted on the bellows in the reverse position. With this arrangement, magnifications of up to 4× were possible. The actual calibration in each test was obtained by taking a photograph of a graduated reticle that was placed on the plane of the droplet stream. The camera and bellows assembly were rigidly mounted on an optical bench which also supported one of the light-illumination systems. The photographic emulsion used in most of the tests was Kodak Tri-X. No special development was found necessary.

4. Data analysis

Displacement data, of the type described above, were obtained for a wide range of droplet sizes and shock-induced velocities. In total, 34 different combinations of these variables were used. The complete data may be found elsewhere (Kim 1977). Here, we show some of these data in graphical form, and describe the procedure used to analyse the data.

The vertical and horizontal droplet displacement measurements result in trajectories of the type shown in figure 9. The figure displays partial trajectories of 87 μm diameter droplets responding to the passage of shock waves of various strengths. The elapsed time since the passage of the shock is given by the number of data points on each

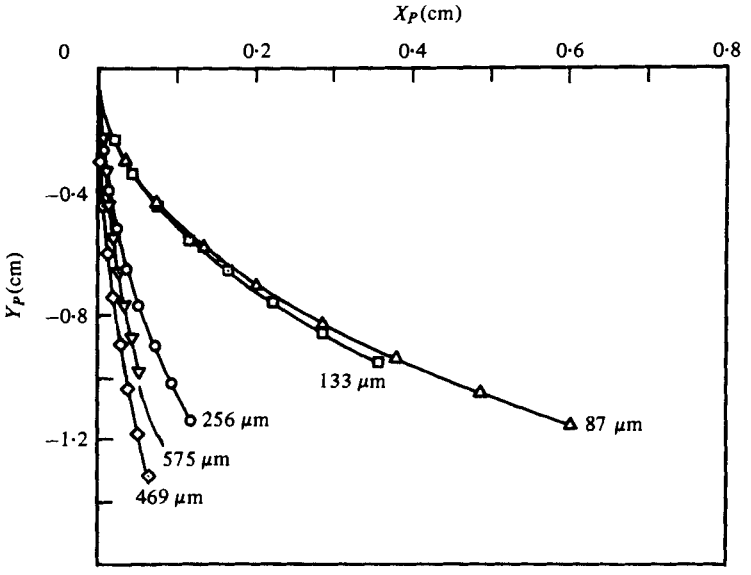

FIGURE 10. Droplet trajectories for $u_2 = 630$ cm s^{-1}.

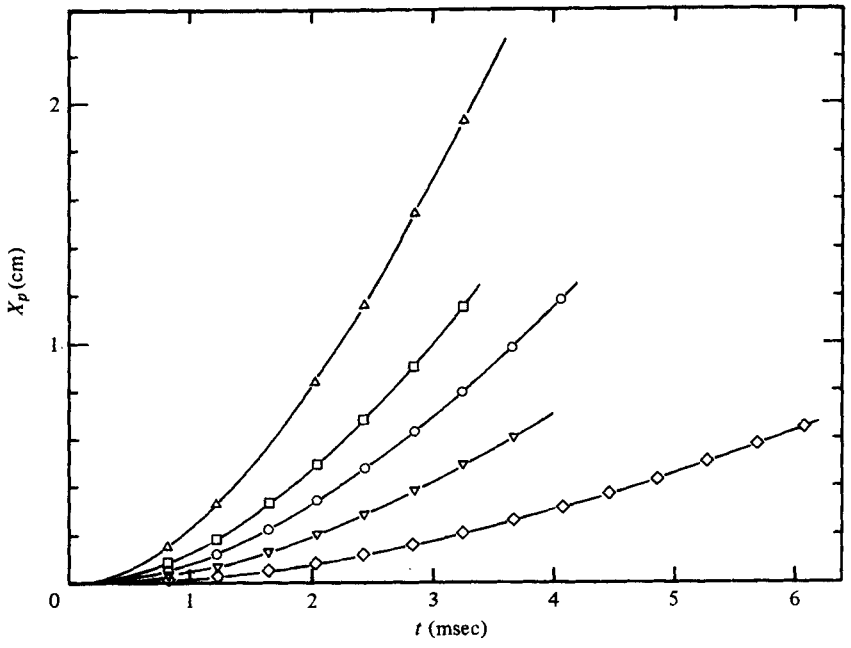

FIGURE 11. Horizontal displacement versus time. $D = 87$ μm. ◇, $u_2 = 264$ cm s^{-1}; ▽, $u_2 = 634$ cm s^{-1}; ○, $u_2 = 991$ cm s^{-1}; □, $u_2 = 1346$ cm s^{-1}; △, $u_2 = 2024$ cm s^{-1}.

trajectory, the maximum elapsed time displayed being 3·25 ms in all trajectories. After the first symbol on each trajectory (obtained at 0·8 ms), the interval between any two data points in a given trajectory is about 0·4 ms. The curves show that, as expected, the horizontal displacement of the droplets increases with flow velocity. In fact, as shown later, the dependence is approximately linear. On the other hand, the vertical

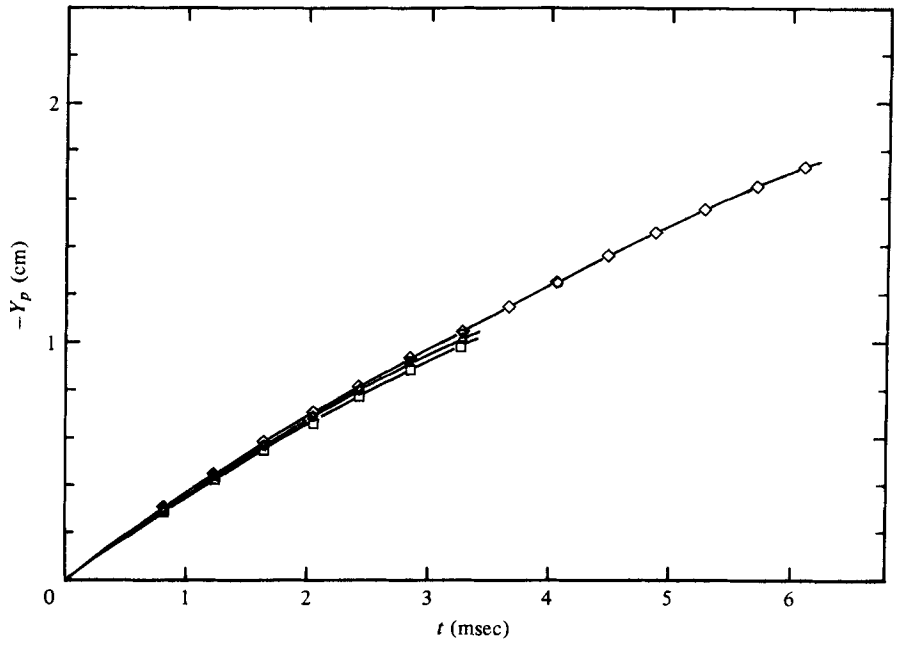

FIGURE 12. Vertical displacement *versus* time. $D = 87$ μm. ◇, $u_2 = 264$ cm s^{-1}; ▽, $u_2 = 634$ cm s^{-1}; ○, $u_2 = 991$ cm s^{-1}; □, $u_2 = 1346$ cm s^{-1}; △, $u_2 = 2024$ cm s^{-1}.

displacement is rather insensitive to the horizontal flow velocity, probably because of the initially high vertical velocity that the droplets have. Since the droplets' diameters were the same in all cases in the figure, this initial vertical velocity was also the same.

Figure 10 shows partial trajectories of different-sized droplets responding to flow velocities of approximately equal magnitude. Since, now, the droplets' diameters are all different, the corresponding initial velocities also differ. This explains why the vertical displacement is not as uniform as that shown in figure 9. The horizontal data display the expected result that smaller droplets are more easily displaced.

The dependence of the motion on time is more easily grasped by plotting, separately, vertical and horizontal displacement data versus time. This is done in figures 11 and 12 for the complete data corresponding to the trajectories of figure 10.

Figure 12 is of interest because it shows that for these droplets the vertical displacement is nearly independent of the shock-induced velocity; i.e. the coupling between horizontal and vertical displacements appears to be small. The probable reasons for this are that the initial vertical velocities of the droplets were nearly the same for these droplets, and that they were relatively large (see table 1).

Data of the type shown in these figures were used to obtain best-fit polynomials in time for the vertical and horizontal displacements. The degree of the polynomials was selected by forming difference tables for the displacements. It was found that the error when fitting the data by means of polynomials was smallest if third-degree polynomials were selected (for details, see Kim, 1977). Thus, the horizontal and vertical displacement data are fitted by expressions of the form

$$X_p = a + bt + ct^2 + dt^3,$$

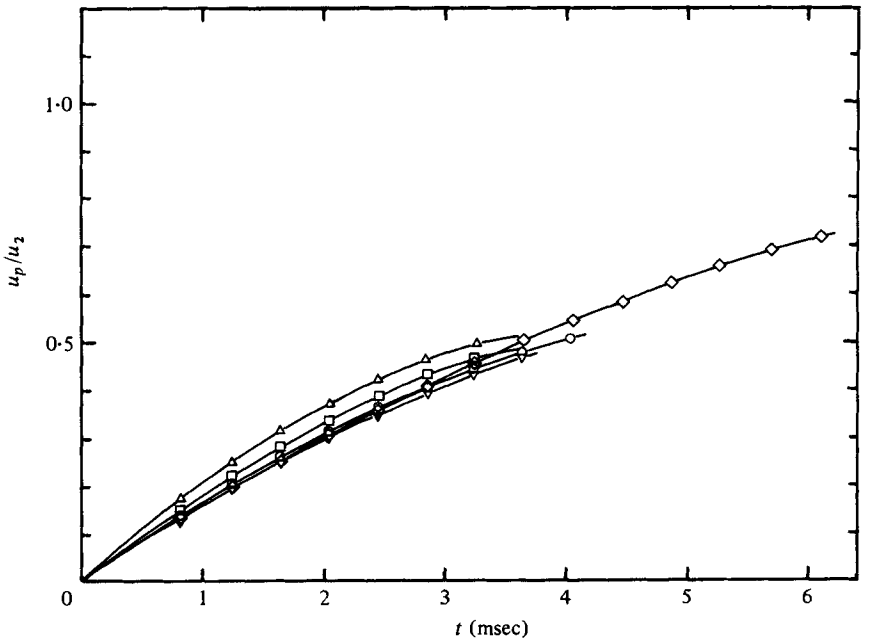

FIGURE 14. Effect of Weber number on velocity ratio u_p/u_2. △, We = 0·317; □, We = 0·142; ○, We = 0·08; ▽, We = 0·035; ◇, We = 0·008.

where the coefficients $a, b, \ldots$, etc., are given together with the data. The polynomials are used to obtain absolute droplet velocity and acceleration components.

As mentioned earlier, the data obtained in this work have a wide range of velocities and droplet sizes. Some of the results were obtained under conditions which resulted in appreciable droplet deformation and oscillation. These data are, therefore, valuable in that they provide additional information about the motion of deforming droplets. Here, however, we would like to select only those data for which droplet deformation is minimal. To do this, photographs of droplets in shock-wave flowfields were obtained for several Weber numbers above and below critical for breakup. Complete sequences of photographs leading to both breakup and to oscillations may be found elsewhere (Kim 1977) and will be reported in the future. Here, in figure 13 (plates 6–8), we show three photographs of similarly sized droplets, obtained at about the same elapsed time, under the effects of shock waves of different strength. The maximum Weber numbers corresponding to each case are 6·3, 1·04 and 0·55. The first case results in breakup ($We_c \approx 3{\cdot}3$), whereas the last two result in droplet oscillation. In the last case, the frequency of oscillation is very nearly equal to the lowest mode of oscillation of a liquid droplet that is derived from linear theory, but the oscillations are not symmetric as that theory predicts. The maximum amplitudes of oscillation in this case amount to about 12 % of the initial diameter.

For Weber numbers below this, the amount of deformation is relatively small, and was impossible to measure with our techniques. Arbitrarily, we used We = 0·15 as the value of the Weber number below which we believe deformation is no longer significant.

One effect of our selection of this Weber number is that the trends displayed by some of the data appear to be similar. For example, figure 14 shows the time variations

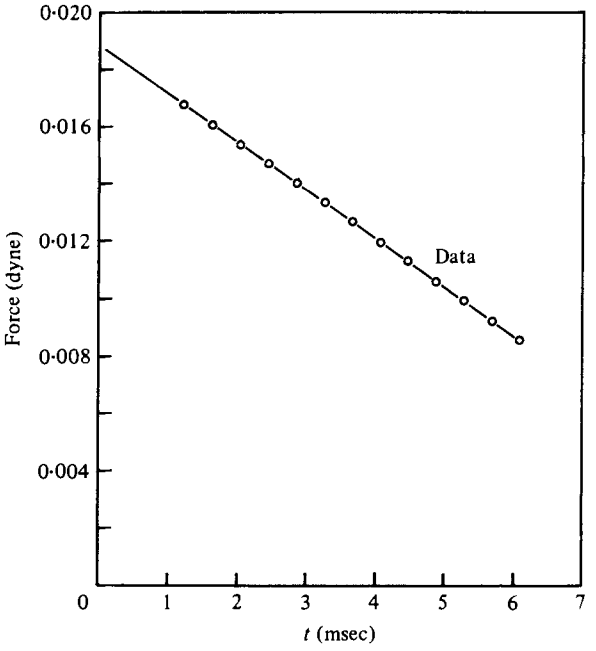

FIGURE 15. Time variations of force on droplets during one test.
$D = 87\ \mu\text{m}$, $u_2 = 264\ \text{cm s}^{-1}$.

of u_p/u_0, formed by taking the derivatives of the polynomials corresponding to the trajectories of figure 10 and by dividing the results by the corresponding flow velocities. It is seen that, except for two cases, the curves nearly coincide. The Weber numbers corresponding to the non-coinciding curves are 0·317 and 0·143. Thus, the departures from similarity may be interpreted as being caused by unequal droplet shapes, i.e. deformation. The effects are more pronounced with the curve for $We = 0{\cdot}317$, but are also present in that with $We = 0{\cdot}143$. This Weber number may, therefore, be taken as the dividing value below which deformation can be assumed to be small. We have, therefore, taken $We = 0{\cdot}15$ as being the maximum Weber number that is used in our drag computations. Of our 34 trajectory data, fifteen have maximum Weber numbers below this number for the entire trajectories. Additional points could have been used by selecting those trajectories which initially had $We > 0{\cdot}15$ but which, owing to a decrease of the relative velocity, would later have $We < 0{\cdot}15$. We did not use such data points because our deformation study had shown that, once the oscillations were excited, they would decay rather slowly.

Because of this limitation, the maximum Reynolds number for which drag data are given here is $Re = 115$. Higher Reynolds number data may also be used, but these will not apply to nearly spherical particles. The final results for the transient drag coefficient were computed from our data by means of (8).

The results of these computations are given in appendix A of Kim (1977), together with other derived quantities. These include the forces on the droplet, and the Reynolds number. Figure 15 shows the magnitude of the fluid forces acting on a droplet during one test. The dependence of this force on time appears to be linear simply because we used third-degree polynomials in time to fit our displacement data. If the line is

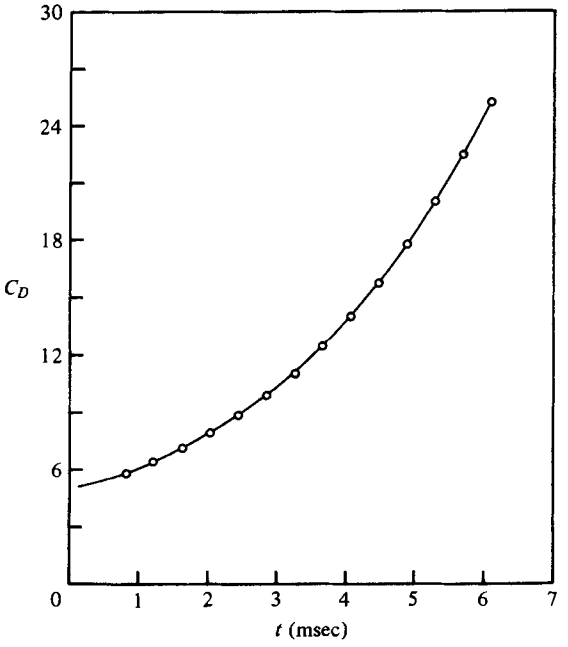

FIGURE 16. Time variations of drag coefficient during one test.
$D = 87\ \mu\text{m}$, $u_2 = 264\ \text{cm s}^{-1}$.

continued to $t = 0$, one may get an idea of the magnitude of the forces that initially act on the droplets. These extrapolated values are probably smaller than the actual, but are nevertheless large. For example, for the case shown in the figure, the force at $t = 0$ is more than 50 times larger than the weight of the droplet. Also, this force is larger, by a factor of 2, than the force that would act on the droplet if the standard drag coefficient were applicable.

Figure 16 shows the time variations of the computed drag coefficient corresponding to the forces of the previous figure.

The changes of relative velocity are basically the same as those of the Reynolds number, which in each test decreases in time. Thus, the relative fluid velocity decreases in time during all of our tests (except, of course, immediately after the passage of the shock, when that velocity increases; this time is, however, very short compared to the time elapsed between the arrival of the shock and the first displacement data point). Finally, in figure 17 we present, as is customarily done, drag coefficient data *versus* the Reynolds number. This figure includes all of our data having maximum Weber numbers less than 0·15. As we pointed out earlier, this factor eliminated from our final results data having larger Reynolds numbers. As we will show below, the lowest and the highest Reynolds number range data shown in figure 17 should also be eliminated, as they may contain large amounts of error.

In order to estimate the overall accuracy of our data, an error-of-magnitude analysis was performed. This included an analysis of the possible errors involved in forming the higher-order derivatives of the displacement polynomials. Such an analysis does not appear to have been performed in past analyses of similar data. As might have been expected, the analysis shows that, for the very low shock-induced velocities, the errors

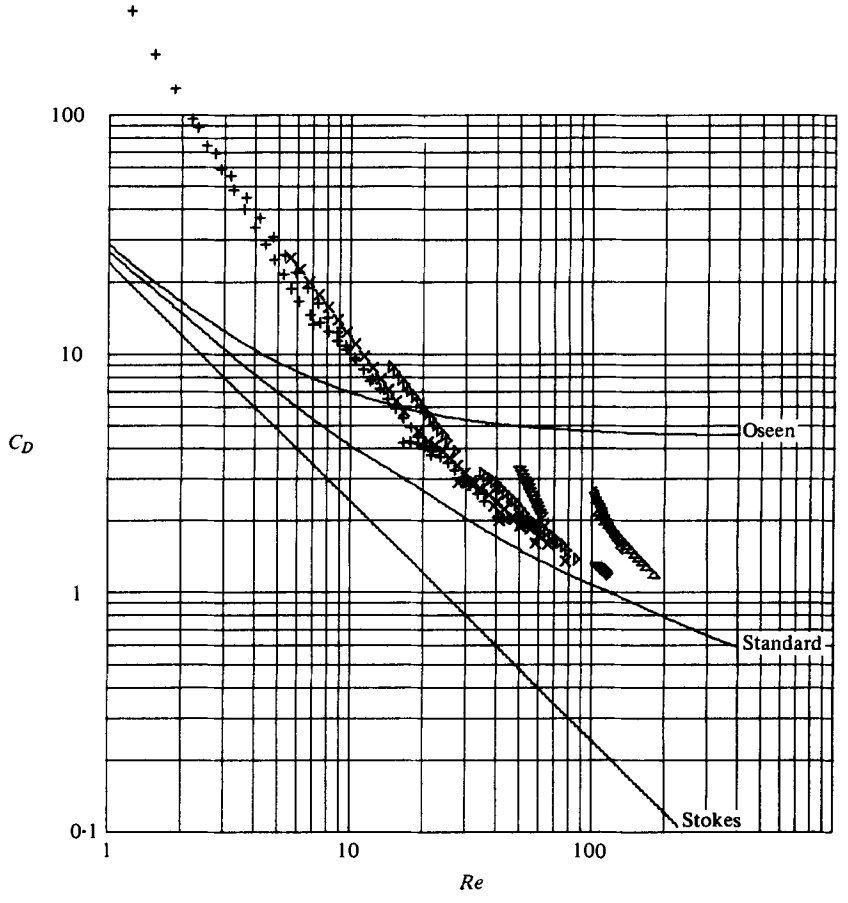

FIGURE 17. Drag coefficient data for $We \leqslant 0{\cdot}15$. +, ×, $D = 87\,\mu$m; ▷, $D = 133\,\mu$m; ▽, $D = 256\,\mu$m; ◁, $D = 470\,\mu$m; △, $D = 575\,\mu$m.

associated with du_p/dt and dv_p/dt may be large. One reason for this is the uncertainty associated with the vertical fluid velocity v. Because this velocity is not usually taken into account in computations of droplet motions similar to this, we describe briefly its origin. First, we recall our definition of $\bar{U}$ as being the fluid velocity at the location corresponding to the instantaneous centre of the sphere if the sphere were not there. Then, if one considers any droplet in the droplet stream, it becomes clear that its neighbours induce, owing to their motion, such a velocity at the location of the droplet under consideration. For example, before the passage of the shock wave, the induced velocity is mainly vertical because the location of the droplet is on the dividing streamline of the flow relative to the other droplets. However, after the passage of the shock, the droplets will acquire a horizontal velocity component, so that the dividing streamline will, in general, be inclined with respect to the droplet stream. It is therefore clear that in our tests the fluid velocity induced by the droplets has two components. Unfortunately, neither component can be experimentally determined. However, if the horizontal velocity induced by the droplets is small compared to the shock-induced velocity, u_2, then we may neglect that component and calculate the other (v) by means of equation (6) with $u = u_2$. This is the assumption that was made in order

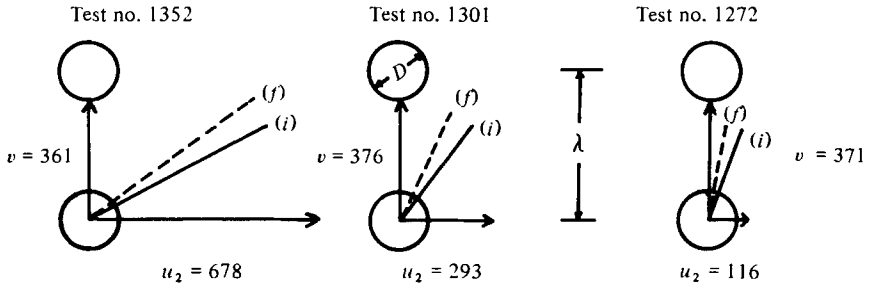

FIGURE 18. Estimated direction of droplet wakes.

to obtain our drag data. The assumption may be accurate for some of the tests, but it is clearly not correct for those having very low values of u_2. Also, in those low shock-induced velocity cases, an additional interaction arises which limits further the accuracy of the data. This may be seen in figure 18, where the initial and final directions of the wakes, calculated from the induced velocities, are schematically shown for three cases. These diagrams show that, for the case having the smallest value of u_2, the droplets basically move in the wakes of their lower neighbours.

The errors in C_D and Re associated with these and other sources of inaccuracy have been estimated, and are given by Kim (1977) for all of the data having Weber numbers smaller than 0·3. For the purposes of computing a C_D, Re correlation, we use only those data for which the fractional error in the Reynolds number is smaller than 15 % throughout a run, and for which the maximum Weber number is 0·15. Seven runs with a total of 82 data points satisfy these criteria. These data and the estimated error bars for a few points in each run are shown in figure 19. The data have been fitted by means of a best fit, second-degree polynomial of the form

$$C_D = b_0 + b_1 Re^{-1} + b_2 Re^{-2}. \tag{11}$$

The coefficients b_n and their standard deviations are given in table 2. The standard deviation of the entire fit is $\sigma = 0{\cdot}39$. While the data are well fitted by (11), the correlation should not, in our view, be used as a drag correlation applicable to unsteady motions unless the unsteadiness is similar to that reported here.

FIGURE 19. Variations of C_D versus Re for runs having estimated errors of the measured Reynolds number smaller than 15 %.

Data symbol	Run no.	D (μm)	U_0 (cm s^{-1})	We(max.)
○	2141	87	264	0·008
▽	1352	86	678	0·040
△	2112	87	634	0·035
▲	2093	87	991	0·080
■	3312	133	635	0·050
●	2064	87	1346	0·143
▼	3293	133	993	0·117

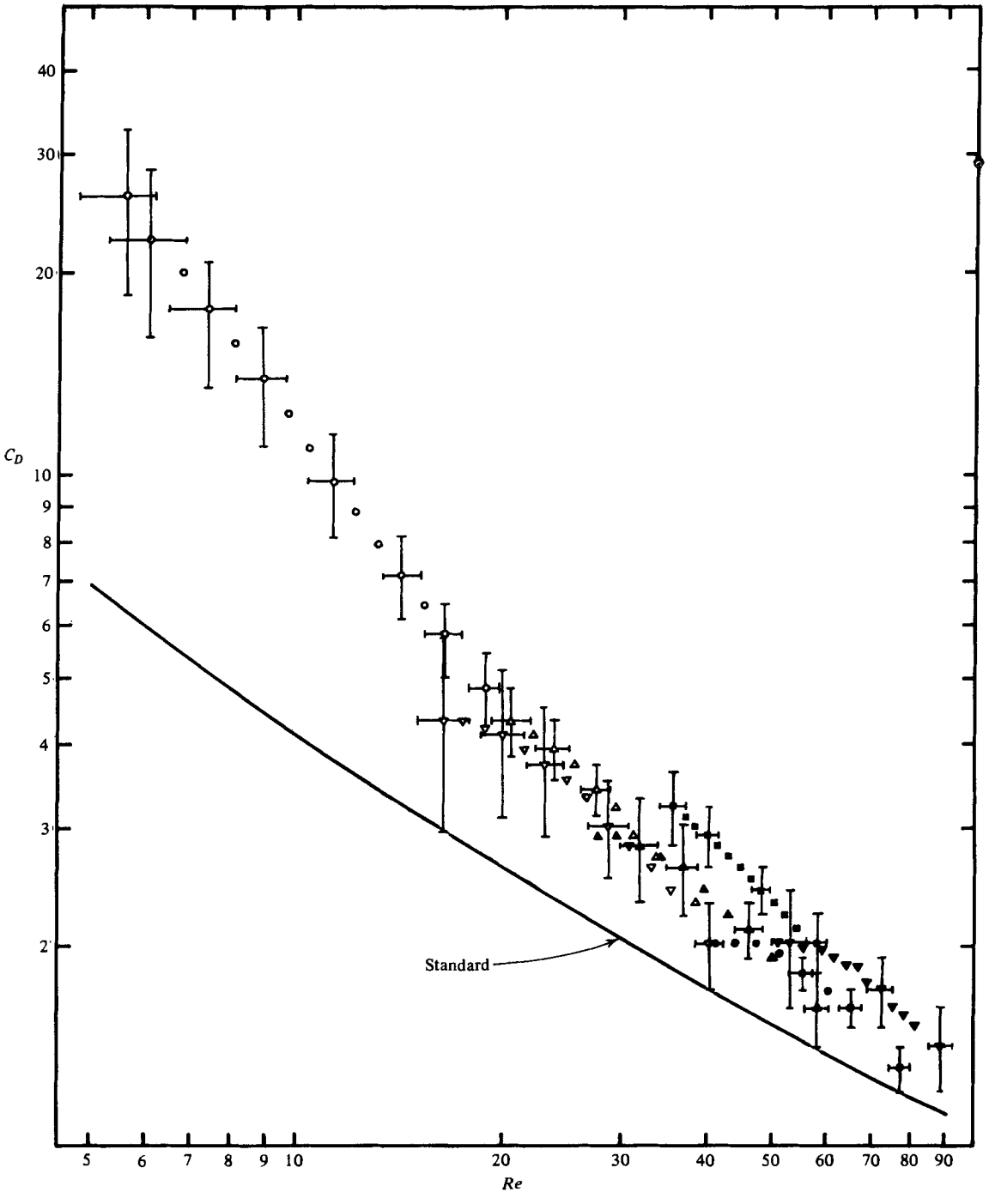

FIGURE 19. For legend see facing page.

n	b_n	Standard error
0	0·69	—
1	56·58	4·48
2	482·49	27·47

TABLE 2. Regression coefficients for drag correlation and their standard errors.

5. Discussion

Also shown in figure 17 are lines representing the well-known Stokes and Oseen drag coefficients, and a line representing the steady or standard drag. This has been drawn by means of the polynomial fits for those data given by Morsi & Alexander (1972). The Stokes and Oseen drags are shown only for illustrative purposes, as the results they represent do not hold for the Reynolds number range shown in the figures. Comparison can be made only with the standard drag, which, however, was obtained by means of steady measurements.

It is seen that our data *always* gives drag coefficients which are larger than the standard. Also, the differences between our data and the standard drag data increase with decreasing Reynolds numbers. We believe that the main reason for these differences is due to the unsteady effects that our droplets experience. Such effects cannot be grasped from figures 17 or 19, for those figures appear to imply that the drag coefficient is a function of the Reynolds number alone. It is clear, however, that unsteadiness, as measured by the acceleration of the droplets, for example, must also appear as a parameter. In fact, an acceleration number defined as $Du_p^{-2}(du_p/dt)$, or its inverse, has been used in the past, but there seems to be some confusion as to whether an absolute or a relative acceleration should be used. However, the fluid forces on the droplet depend primarily on the velocity of the fluid relative to the droplet. Also, changes in that velocity may affect the structure of the recirculating region in the rear of the sphere and, therefore, the drag. Accordingly, we measure the effects of unsteadiness in terms of the changes of $U_r = |\bar{U} - \bar{u}_p|$ – the magnitude of the fluid velocity as seen by an observer moving with the sphere. Thus, instead of the above acceleration number we use

$$\frac{D}{U_r^2}\frac{dU_r}{dt}.$$

This parameter may also be established directly from the equations of motion when these are referred to axes moving with the sphere. Other parameters that are needed to specify the drag coefficient on a droplet translating in an unbounded fluid include the Reynolds number, the Weber number, the ratio of fluid density to sphere density, and the Mach number behind the shock wave, M_2.† Since we are considering only those data having minimal deformation, we can delete the Weber number from this list.

† This list ignores several other effects which may be present, such as droplet evaporation, internal circulation, and droplet rotation. Evaporation may be ruled out as its effects would be significant only in a time scale which is large when compared to the test time. On the other hand, internal circulation is established in a time of the order of R^2/ν_{water}, which, for our smallest droplets, is comparable to the test time. Further, owing to their method of production, the droplets' surfaces were probably free from impurities, and hence free to move. Therefore, circulation within the droplets probably occurred during the tests. However, its effects on the drag as well as on those due to possible rotation could not be assessed.

Further, since our shocks are quite weak, compressibility effects may be neglected. Therefore, the drag coefficient for a rigid sphere which is translating unsteadily in an unbounded incompressible fluid that has been set impulsively into motion, may be expressed as

$$C_D = C_D\left(Re, \frac{D}{U_r^2}\frac{dU_r}{dt}, \frac{\rho_0}{\rho_p}\right). \tag{12}$$

This differs from the steady drag C_{DS} in that C_{DS} depends only on the Reynolds number. Therefore if C_D is to agree with its steady counterpart when $dU_r/dt = 0$, it is necessary that the dependence on the density ratio vanishes in that condition. It is therefore evident that the dependence on the last two parameters in (12) must appear through a single group in which functions of these parameters appear as factors such that the group vanishes when $dU_r/dt = 0$. For simplicity we take the combination†

$$A = \left(\frac{\rho_p}{\rho_0} - 1\right)\frac{D}{U_r^2}\frac{dU_r}{dt}, \tag{13}$$

although others are possible. This form has the additional advantage of vanishing, as it should, when the densities are equal. With this definition of A, we write (12) in the form

$$C_D = C_D(Re, A). \tag{14}$$

The dependence of C_D on A for a given Reynolds number is, of course, unknown, but some of its features may sometimes be deduced by considering the changes of the relative fluid velocity past the droplet. Consider first the case $A = 0$ for some fixed Reynolds number Re. Here C_D is given by its steady value $C_{DS}(Re)$ and this is given by the sum of a friction drag and a pressure drag. Now, suppose that the Reynolds number is such that a recirculation region exists‡ on the rear side of the sphere. Then the pressure drag coefficient is a significant fraction of the total drag. Therefore, if the size of the recirculating region changes, the change should be reflected on the total drag coefficient, provided, of course, that the related changes of the friction drag are such that they do not mask those of the pressure drag.

Consider now another case having instantaneously the same Reynolds number as that of the steady case considered above, but having $dU_r/dt > 0$. This acceleration of the free-stream velocity might be associated with a more favourable pressure gradient (relative to the steady case). This gradient would result in a smaller recirculation region, and therefore in a smaller drag. Similarly, when $dU_r/dt < 0$, the pressure gradient may be more adverse so that the recirculating region and the drag are expected to be then larger than their steady values. Thus, if the changes of pressure drag predominate, then, for a given Reynolds number, the drag coefficient is expected to be smaller or larger than the steady value depending on whether A is positive or negative, respectively.§

Our experimental results do not depend on this argument, and may therefore be

† Form suggested by a reviewer.

‡ The Reynolds number for which the recirculation region does not exist is not known. However, some recent experimental results (Nakamura 1976) show that a recirculating eddy exists for Reynolds number as low as 7·3, the lowest Reynolds number tested.

§ This argument is not expected to apply to all unsteady motions; for example to those motions where separation does not occur.

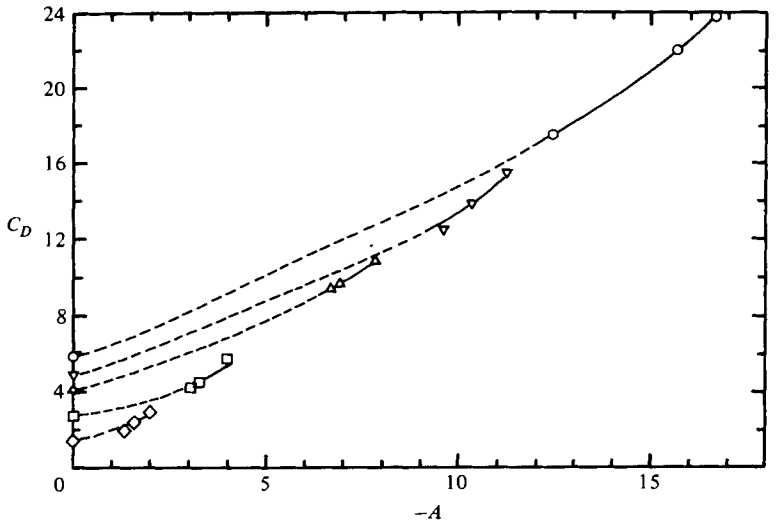

FIGURE 20. Variations of C_D versus $-A$ for several Reynolds numbers. ○, $Re = 6$; ▽, $Re = 8{\cdot}1$; △, $Re = 10{\cdot}5$; □, $Re = 20{\cdot}5$; ◇, $Re = 51$.

used to test it.† Unfortunately, in all of our experiments the quantity dU_r/dt was negative, so that only part of the argument can be tested. Further, the number of data points having the same instantaneous Reynolds number, but having different values of A, is small. Nevertheless, our results display the expected trend, as may be seen in figure 20, where experimental values of C_D (including steady values from the literature) are plotted versus $-A$ for several Reynolds numbers. All of these data clearly show that as the relative deceleration increases, the measured values of C_D increase relative to the steady values. Also shown in figure 20 are dotted lines connecting our constant Reynolds number drag data with the corresponding steady values. This line does not represent experimental or theoretical data, but it is clear that, if experiments were performed for continuously decreasing values of $|A|$, then curves not too unlike those shown in the figure would be obtained.

The data shown in figure 20 may also be used to obtain some information about the dependence of C_D on both Reynolds number and on the relative acceleration parameter. This is done by subtracting from each data point in the figure the steady value, C_{DS}, corresponding to that particular Reynolds number. The result is shown in figure 21. It may be seen that the quantity $C_D(Re, A) - C_{DS}(Re)$ appears to be independent of the Reynolds number, i.e. $C_D = C_{DS} + f(A)$, where $f(A)$ is a function of A alone. Also shown in figure 21 is the line $g(A) = -A$. With the exception of points having small values of $C_D - C_{DS}$ this line agrees surprisingly well with the data.‡ Further, when the values of

† It is not possible to compare the predicted trend with the results of numerical calculations or the flow around impulsively started spheres that are available in the literature (Rimon & Cheng 1969; Dennis & Walker 1971, 1972) because the pressure and friction contributions to the drag after separation are not given in any of these papers.

‡ Data points having small values of $C_D - C_{DS}$ should also be correlated with A. This may be seen as follows. Small values of $C_D - C_{DS}$ occur for small values of A, and for these a power series expansion of (14) in the vicinity of $A = 0$ gives $C_D = C_{DS} + h(Re)\, A + \ldots$. The departure from a linear dependence of those points is probably due to the errors in C_D, which are then large relative to the values of $C_D - C_{DS}$ (see figure 19).

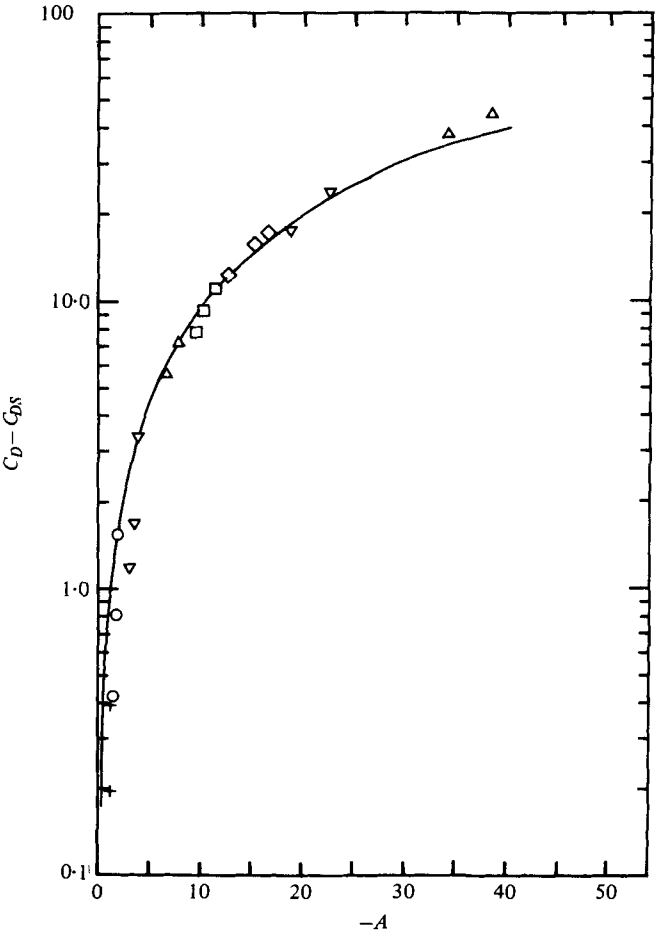

FIGURE 21. Difference between measured drag and steady drag as a function of deceleration. ——, $g(-A) = -A$. ▷, $Re = 3{\cdot}2$; ◁, $Re = 4{\cdot}7$; ◇, $Re = 6$; □, $Re = 8{\cdot}1$; △, $Re = 10{\cdot}5$; ▽, $Re = 20{\cdot}5$; ○, $Re = 51$; +, $Re = 77$.

$C_D - C_{DS}$ for the data points shown in figure 19 are plotted versus A, exactly the same pattern is obtained. Therefore, within the accuracy of our experiments, we can write

$$C_D = C_{DS} - K\left(\frac{\rho_p}{\rho_0} - 1\right)\frac{D}{U_r^2}\frac{dU_r}{dt}, \tag{15}$$

where the constant K is nearly unity. This equation represents an important result of this work in that it gives explicitly the dependence on acceleration of the drag coefficient for rigid spheres accelerating in the uniform flow behind a weak shock wave. However, while it might also provide a fair model for C_D in similar types of unsteady motions, it does not apply to others. For example, the time average of the drag coefficient on a sphere executing translational harmonic oscillations is, according to (15), equal to C_{DS} whereas the recent measurements of Karanfilian & Kotas (1978) show that it is larger than C_{DS}.

The authors are grateful to Professor G. K. Batchelor for his illuminating comments on our drag measurements.

This research was supported by the National Science Foundation under Grants NSF-GK 40007 and NSF ENG 76-15045.

REFERENCES

ADAM, J. R., CATANEO, R. & SEMONIN, R. G. 1971 The production of equal and unequal size droplet pairs. *Rev. Sci. Instr.* **42**, 1847–1849.

BEARD, K. V. & PRUPPACHER, H. R. 1969 A determination of the terminal velocity and drag of small water drops by means of a wind tunnel *J. Atmos. Sci.* **26**, 1066–1072.

DENNIS, S. C. R. & WALKER, J. D. A. 1971 The initial flow past an impulsively started sphere at high Reynolds numbers. *J. Engng Math.* **5**, 263–278.

DENNIS, S. C. R. & WALKER, J. D. A. 1972 Numerical solutions for time-dependent flow past an impulsively started sphere. *Phys. Fluids* **15**, 517–525.

HANSON, A. R., DOMICH, E. G. & ADAMS, H. S. 1963 Shock tube investigation of the breakup of drops by air blasts. *Phys. Fluids* **6**, 1070–1080.

HILL, M. K. 1973 Behavior of spherical particles at low Reynolds numbers in a fluctuating translational flow. Ph.D. thesis, California Institute of Technology.

HOGLUND, R. F. 1962 Recent advances in gas particle nozzle flows. *J. Am. Rocket Soc.* **32**, 662–671.

HUGHES, R. R. & GILLILAND, E. R. 1952 The mechanics of drops. *Chem. Engng Prog.* **48**, 497–504.

INGEBO, R. D. 1956 Drag coefficients for droplets and solid spheres in clouds accelerating in air streams. *N.A.C.A. Tech. note* TN 3762.

KARANFILIAN, S. K. & KOTAS, T. J. 1978 Drag on a sphere in unsteady motion in a liquid at rest. *J. Fluid Mech.* **87**, 85–96.

KELLER, J., RUBINOW, S. I. & TU, Y. O. 1973 Spatial instability of a jet. *Phys. Fluids* **16**, 2052–2055.

KIM, S. S. 1977 An experimental study of droplet response to weak shock waves. Ph.D. thesis, Rutgers University.

LANGMUIR, I. 1948 The production of rain by a chain-reaction in cumulus clouds at temperatures above freezing. *J. Met.* **5**, 175–192.

LUNNON, R. G. 1926 Fluid resistance to moving spheres. *Proc. Roy. Soc.* A **110**, 302–326.

MARBLE, F. E. 1963 Nozzle contours for minimum particle-lag loss. *A.I.A.A. J.* **1**, 2793–2801.

MASON, B. J. 1971 *The Physics of Clouds.* Oxford University Press.

MORSI, S. A. & ALEXANDER, A. J. 1972 An investigation of particle trajectories in two-phase flow systems. *J. Fluid Mech.* **55**, 193–208.

NAKAMURA, I. 1976 Steady wake behind a sphere. *Phys. Fluids* **19**, 5–8.

OCKENDON, J. R. 1968 The unsteady motion of a small sphere in a viscous fluid. *J. Fluid Mech.* **34**, 229–239.

ODAR, F. & HAMILTON, W. S. 1964 Forces on a sphere accelerating in a viscous fluid. *J. Fluid Mech.* **18**, 302–314.

PEARCEY, T. & HILL, G. W. 1956 The accelerated motion of droplets and bubbles. *Austr. J. Phys.* **9**, 19–30.

PRUPPACHER, H. R., LE CLAIR, B. P. & HAMIELEC, A. E. 1970 Some relations between drag and flow pattern of viscous flow past a sphere and a cylinder at low and intermediate Reynolds numbers. *J. Fluid Mech.* **44**, 781–790.

REICHMAN, J. M. 1973 A study of the motion, deformation and breakup of accelerating water droplets. Ph.D. thesis, Rutgers University.

REICHMAN, J. M. & TEMKIN, S. 1974 A study of the deformation and breakup of accelerating water droplets. *Proc. Int. Coll. on Drops and Bubbles*, 28–30 August, Pasadena, California, pp. 446–464.

RIMON, Y. & CHENG, S. I. 1969 Numerical solution of a uniform flow over a sphere at intermediate Reynolds numbers. *Phys. Fluids* **12**, 949–959.

ROOS, F. W. & WILLMARTH, W. W. 1971 Some experimental results on sphere and disk drag. *A.I.A.A. J.* **9**, 285–291.

RUDINGER, G. 1969 Effective drag coefficients for gas–particle flow in shock tubes. *Proj. Squid Tech. Rep.* CAL-97-PU.

SAFFMAN, P. G. & TURNER, J. S. 1956 On the collision of drops in turbulent clouds. *J. Fluid Mech.* **1**, 16–30.

SELBERG, B. P. & NICHOLLS, J. A. 1968 Drag coefficient of small spherical particles. *A.I.A.A. J.* **6**, 401–408.

TEMKIN, S. 1970 Droplet agglomeration induced by weak shock waves. *Phys. Fluids* **13**, 1639–1641.

TEMKIN, S. 1972 On the response of a sphere to an acoustic pulse. *J. Fluid Mech.* **54**, 339–349.

TEMKIN, S. & REICHMAN, J. M. 1972 A new technique to photograph small particles in motion. *Rev. Sci. Instr.* **43**, 1456–1459.

TOROBIN, L. B. & GAUVIN, W. H. 1959 Fundamental aspects of solids–gas flows. III. Accelerated motion of a particle in a fluid. *Can. J. Chem. Engng* **37**, 224–236.

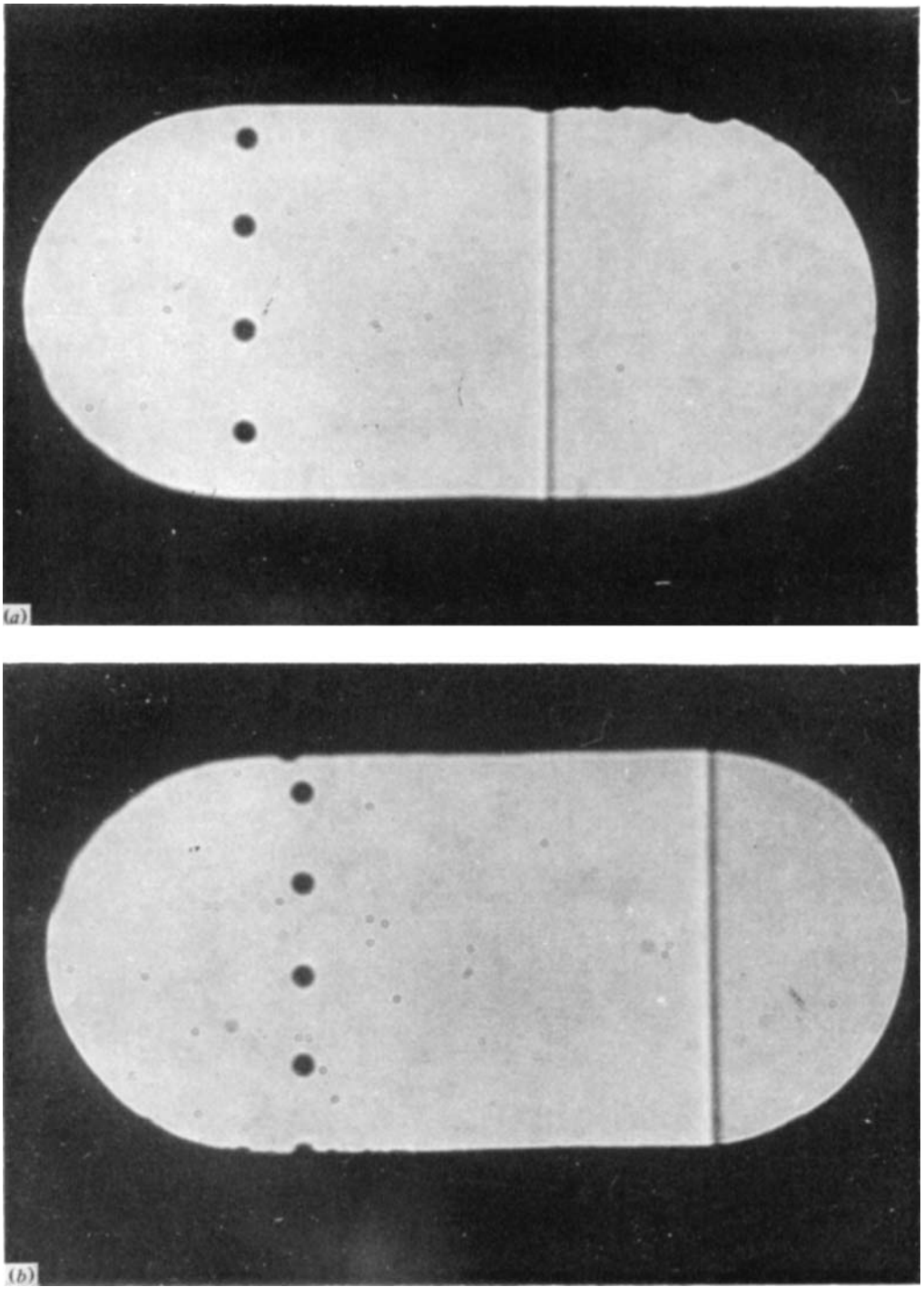

FIGURE 2. Wavefront passage. (*a*) $t = 24{\cdot}9\ \mu$s, (*b*) $t = 33{\cdot}4\ \mu$s.

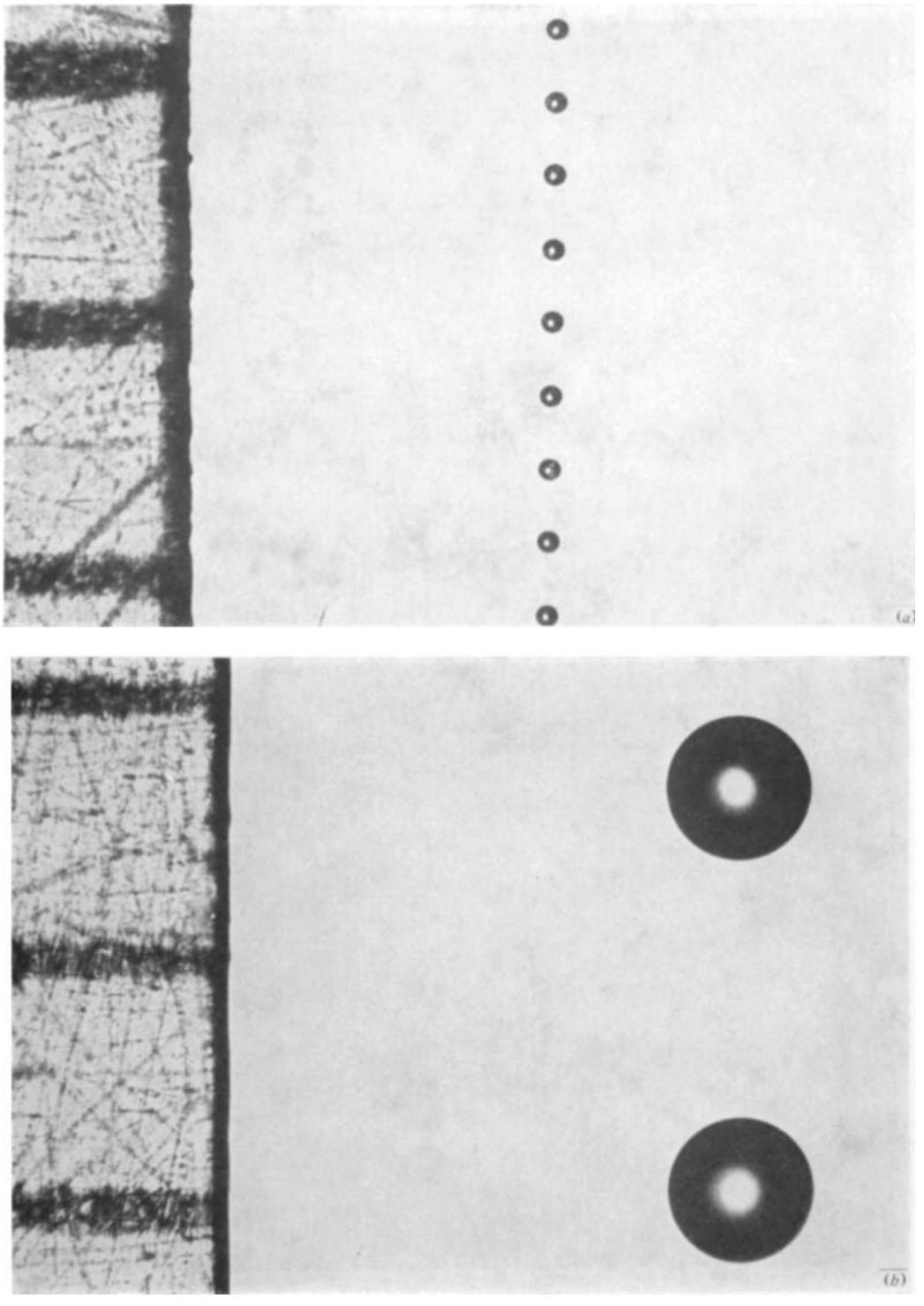

FIGURE 4. Streams of water droplets. (*a*) $D = 87\ \mu$m, (*b*) $D = 575\ \mu$m.

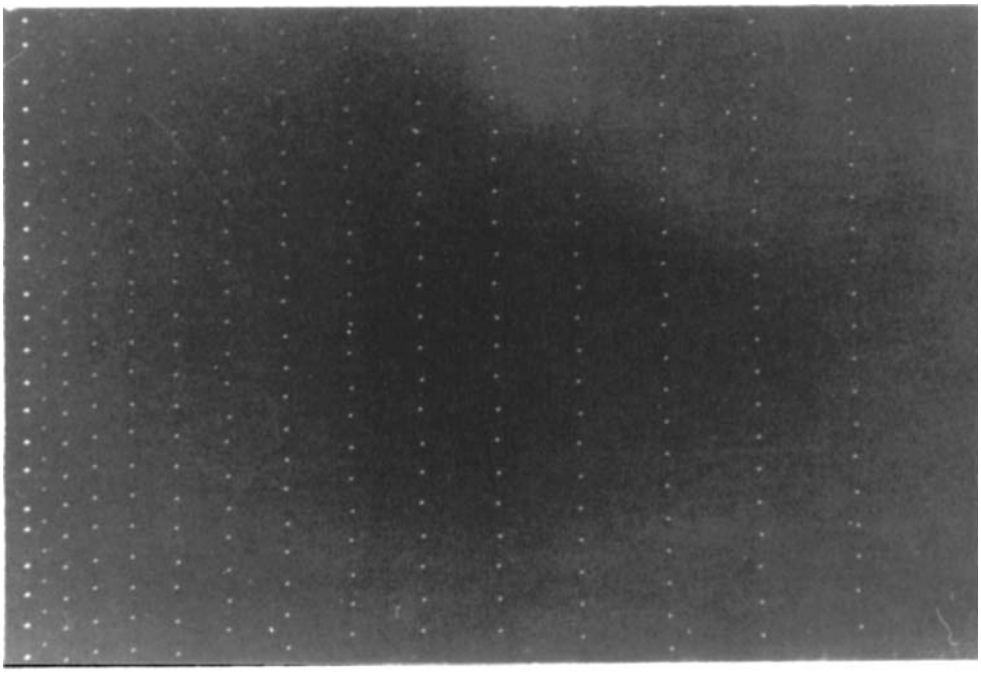

FIGURE 6. Scattered-light photograph. $D = 87\ \mu$m, $u_2 = 264$ cm s^{-1}.

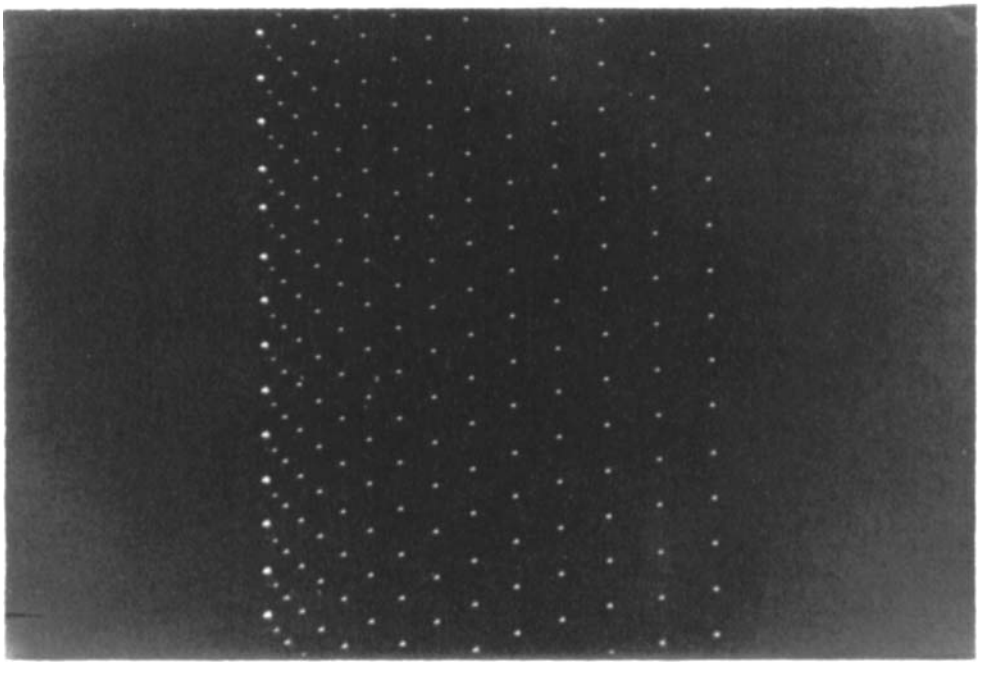

FIGURE 7. Scattered-light photograph. $D = 133\ \mu$m, $u_2 = 264$ cm s^{-1}.

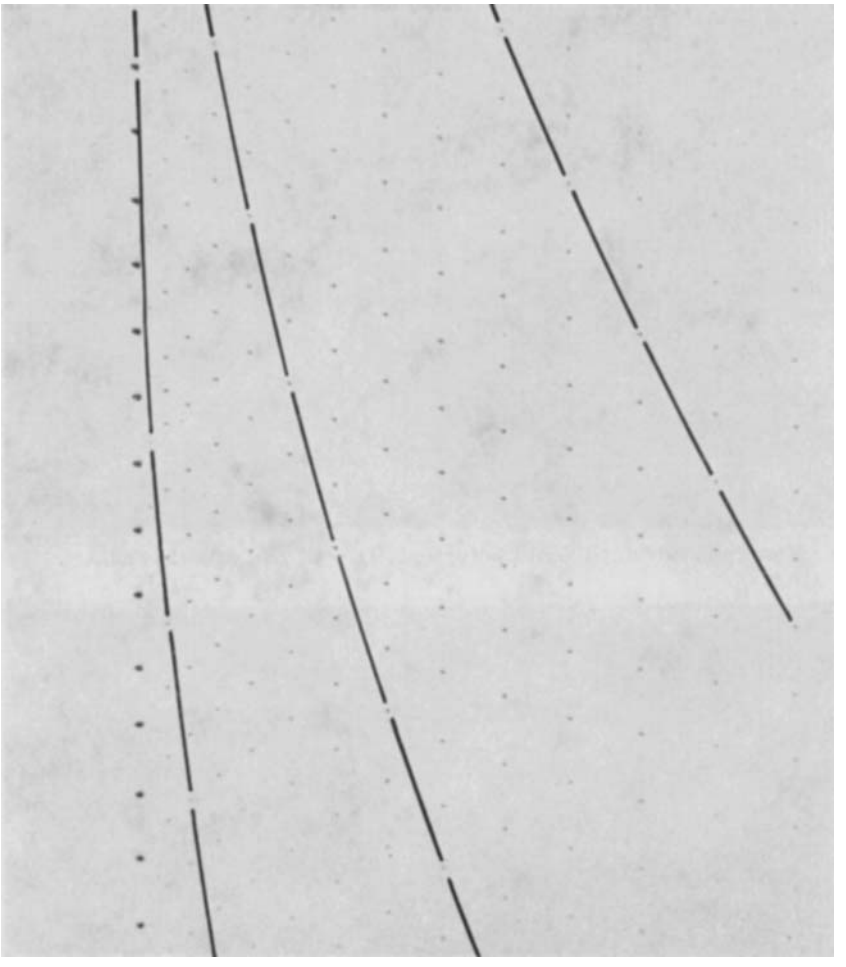

FIGURE 8. Droplet trajectories in a typical test.

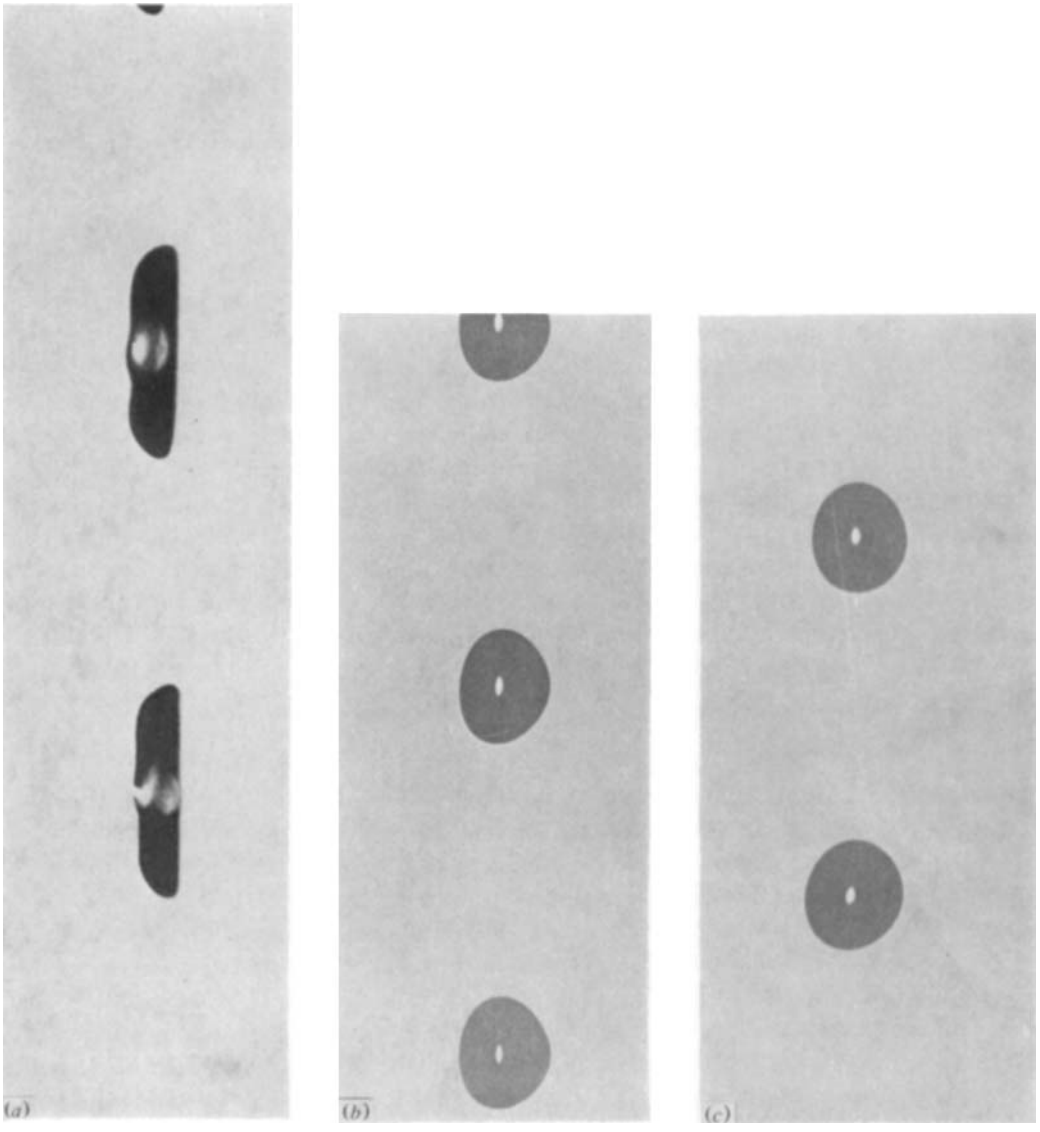

FIGURE 13. Deformation at $t \approx 0{\cdot}450$ ms. (*a*) $We = 6$, (*b*) $We = 1{\cdot}04$, (*c*) $We = 0{\cdot}55$.